# scientific reports

OPEN

# Cerium oxide-embedded gold nanoparticles loaded with astragaloside IV for bladder cancer therapy

Xiaoyu Zhu[1,4], Xuelai Yin[1,4], Lin Niu[2,4], Gang Yang[1], Yanchao Xu[1], Yajie Yu[1], Yidong Cheng[1], Xiaolun Ma[3], Ting Huang[1], Wu Wei[1] & Fangze Tao[1✉]

In bladder cancer, metabolic dysregulation of reactive oxygen species (ROS) promotes malignant transformation through oxidative DNA damage while concurrently activating pro-survival pathways such as NF-κB. To address this, we developed a synergistic therapeutic platform by incorporating gold nanoparticles into cerium oxide nanostructures ($Au/CeO_2$) with enhanced antioxidant activity, followed by loading with astragaloside IV ($Au/CeO_2@As$). The core-shell structured $Au/CeO_2@As$ nanocomposites demonstrated remarkable pro-apoptotic effects, exhibiting a 5.11-fold increase in apoptosis induction compared to free astragaloside IV alone. Subsequent cell proliferation assays confirmed the system's ability to effectively inhibit tumor cell migration and proliferation. Mechanistic investigations through qPCR and Western blot analyses revealed that $Au/CeO_2@As$ mediates its antitumor effects through coordinated regulation of the STAT3 and NF-κB signaling pathways, leading to significant tumor cell damage. Importantly, the $Au/CeO_2@As$ nanocomposites did not exhibit significant cytotoxicity while demonstrating excellent therapeutic efficacy. These findings collectively establish $Au/CeO_2@As$ as a highly promising nanotherapeutic candidate for bladder cancer treatment, offering both targeted ROS modulation and specific pathway regulation capabilities.

Bladder cancer is a common malignant tumor of the urinary system with a relatively high incidence. According to the 2020 global cancer statistics, bladder cancer accounted for 4.4% of newly diagnosed malignant tumors in men, ranking as the 6th most prevalent[1]. The five-year survival rate for early-stage bladder cancer is relatively high, reaching 97%. However, once metastasis occurs, the rate drops drastically to merely 8%[2,3]. Bladder cancer is primarily classified into non-muscle-invasive bladder cancer (NMIBC) and muscle-invasive bladder cancer (MIBC)[4,5]. NMIBC typically presents as papillary lesions, mostly low-grade, with a favorable prognosis, whereas MIBC is more aggressive and has a poorer prognosis[6,7]. The pathogenesis of bladder cancer is complex and associated with various factors such as smoking, chronic inflammation, and exposure to chemical carcinogens[8]. Due to its high recurrence rate and therapeutic challenges, bladder cancer remains a critical area of oncological research.

Currently, transurethral resection of bladder tumor (TURBT) is the main treatment method, but it carries the risk of tumor cell implantation and recurrence[7]. Therefore, postoperative intravesical chemotherapy is often used to reduce the recurrence rate. In addition, radical cystectomy (RC) is the standard treatment, but it has a significant impact on the patient's quality of life, with potential postoperative complications such as urinary incontinence and sexual dysfunction[9]. Emerging treatment methods, such as immunotherapy and targeted therapy (e.g., PD-1/PD-L1 inhibitors), are continuously emerging and offer new hope for patients with advanced bladder cancer[10,11]. Despite continuous updates in treatment methods, the overall prognosis of bladder cancer remains unsatisfactory[7].

Nanomaterials offer a multifunctional platform for improving bladder cancer treatment by enhancing drug delivery and reducing side effects, holding promise for more effective and personalized bladder cancer therapies

[1]Department of Urology, Nanjing Hospital of Traditional Chinese Medicine, Nanjing University of Chinese Medicine, Nanjing 210096, P. R. China. [2]Department of Urology, Jiangsu Provincial Hospital of Traditional Chinese Medicine, Nanjing University of Chinese Medicine, Nanjing 210096, P. R. China. [3]Kunshan Hospital of Integrated Traditional Chinese and Western Medicine, Suzhou 215300, P. R. China. [4]These authors equally contributed to this work: Xiaoyu Zhu, Xuelai Yin and Lin Niu. ✉email: taofangze1981@163.com

in the future[12,13]. In addition to enhancing drug delivery and reducing side effects, nanomaterials can adhere to the bladder mucosa, thereby reducing drug loss caused by urine flushing. For example, Chen et al. designed an adhesive liposome that significantly extended the retention time in the bladder and enhanced drug penetration by surface modification with chitosan and hyaluronic acid, thereby increasing the drug concentration in tumor tissue[14,15]. Huang et al. successfully synthesized gold nanoparticles loaded with doxorubicin (AuNPs-DOX) and modified them with folic acid, which efficiently delivered doxorubicin to bladder cancer tissues and significantly enhanced the antitumor efficacy[16]. The ability of cerium (Ce), particularly in its nanoparticle form ($CeO_2$ NPs), to regulate intracellular reactive oxygen species (ROS) levels is primarily attributed to its unique mixed valence state ($Ce^{3+}/Ce^{4+}$) and the resulting enzyme-like catalytic activity[17,18]. Seal et al. investigated the mechanism of $CeO_2$ in bladder cancer, revealing that it increases intracellular ROS levels, induces DNA damage, mitochondrial dysfunction, and ultimately triggers apoptosis, thereby achieving therapeutic effects against bladder cancer[19]. He et al. selectively deposited cerium dioxide ($CeO_2$) at the tips of gold nanorods (Au NRs), forming dumbbell-shaped hybrid nanozymes. These nanostructures were further loaded with gemcitabine (GEM), enabling Au-mediated photothermal therapy while $CeO_2$ amplified drug efficacy through ROS Generation. The combined treatment achieved complete tumor elimination in 60% of mice[20,21]. Nanocarriers, by virtue of their unique drug delivery properties, provide a critical breakthrough for innovative treatment strategies in bladder cancer.

Astragaloside IV (As-IV), the primary bioactive constituent extracted from the traditional Chinese herb Astragalus membranaceus, exhibits broad-spectrum immunomodulatory properties. Recent studies have demonstrated its potential therapeutic value in bladder cancer treatment. However, its clinical application is limited by poor oral bioavailability ($< 5\%$), necessitating the use of nanocarriers to enhance drug delivery efficiency[22]. To improve the solubility and bioavailability of As-IV, researchers have developed nano-carrier delivery systems. For instance, polycaprolactone-polyethylene glycol (PCL-PEG) copolymer based nano-micelles can effectively encapsulate As-IV and improve its solubility[23].

In this study, we designed a core-shell structured gold-embedded cerium oxide nanoparticle ($Au/CeO_2$) loaded with As-IV for bladder cancer treatment. The porous $Au/CeO_2$ architecture provides high surface-area-to-volume catalytic sites, facilitating the $Ce^{3+}/Ce^{4+}$ redox cycle and enhancing the antioxidant enzyme-mimetic activity of cerium oxide. The $Au/CeO_2$ component generates reactive oxygen species (ROS) to induce apoptosis, while As-IV modulates cell proliferation via NF-κB pathway regulation. Notably, the $Au/CeO_2$@As system demonstrates excellent biocompatibility. These results collectively indicate that $Au/CeO_2$@As nanoparticles represent a promising therapeutic agent for bladder cancer.

## Experimental

### Synthesis of Au/CeO$_2$ nanoparticles

$Au/CeO_2$ was synthesized according to previously reported methods[24]. Specifically, add HAuCl4 (0.024 M, 600 μL) and $Ce(NO_3)_3$ (0.1 M, 1400 μL) to ice-cold water (50 mL). Ascorbic acid was employed as the reducing agent to reduce chloroauric acid ($HAuCl_4$) to form gold nanoparticles. Quickly introduce an ammonia solution (64 μL of 25–28% ammonia solution dissolved in 3 mL of $H_2O$), stir the mixture, and then add the $Ce(NO_3)_3$ solution (0.0467 M, 3000 μL). After stirring for 15 min at 10 °C, centrifuge the mixture at 10,000 g for 60 min. Wash the product three times with pure water, and collect the final $Au/CeO_2$ nanoparticles.

### Au/CeO$_2$@As nanoparticle synthesis

The obtained $Au/CeO_2$ nanoparticles are mixed with As-IV in a 1:10 ratio and incubated on a shaker at room temperature for 4 h. After centrifugation and washing, the final product, $Au/CeO_2$@As nanoparticles, are obtained.

### In vitro characterization

The hydrodynamic diameter and zeta potential of the $Au/CeO_2$ nanoparticles were measured following dispersion in deionized water using the Nano-ZS ZEN3600 (Malvern). The morphology of the nanoparticles was characterized by transmission electron microscopy (Hitachi H-7000FA) and high-resolution transition electron microscopy (HR-TEM) (Jeol2100f). The element component of the samples was measured with scanning electron microscopy (SEM, Ultra Plus, Carl Zeiss, Germany). Ultraviolet-visible (UV-vis) absorption spectra were recorded on a UV-vis spectrophotometer (Shimadzu UV-3600). The drug loading capacity of the nanoparticles was determined using high-performance liquid chromatography (HPLC; Agilent Technologies 1260 Infinity II). Drug Loading = (Mass of Encapsulated Drug)/(Total Mass of Nanoparticles) × 100%.

### Cell culture

The MB49 cell line used in this study is a murine bladder cancer cell line, while the MBEC cells are murine bladder epithelial cells. Both cell lines were purchased from Yuuchi (Shanghai) Biotechnology Co., Ltd. The cells were cultured in DMEM (Dulbecco's Modified Eagle Medium) medium supplemented with 10% fetal bovine serum (FBS) and 1% penicillin/streptomycin at 37 °C under 5% $CO_2$. Subculturing was performed every two days (upon reaching 80–90% confluency) using trypsin.

### Cell live/dead staining

Cell viability was assessed using calcein-AM/PI staining (Thermo Fisher). MB49 cells in the logarithmic growth phase were seeded in a 12-well plate at a density of $1 \times 10^5$ cells well[1]. After reaching the desired density, the culture medium was replaced with fresh medium free of nanomaterials. Following 24 h of incubation, cells were stained with 2 μM calcein-AM and 4 μg/mL PI for 20 min and then imaged under a fluorescence microscope. Live cells (green fluorescence) and dead cells (red fluorescence) were quantified using ImageJ.

### In vitro cytotoxicity assay

CCK-8 method (Dojindo) was used to measure cell viability. Specifically, the logarithmic growth phase cells were inoculated in 96-well plates ($1 \times 10^4$ cells/well) for incubating overnight, treated with different nanomaterials for 24/48 hours. Afterward, the cells were then incubated with a fresh serum-free medium containing 10 μL CCK-8 in the dark for 2 h. Absorbance was measured at 450 nm using an enzyme-labeled reader. Relative cell viability is calculated by following formula:

$$\text{Cell viability}(\%) = (\text{OD}_{\text{sample}} - \text{OD}_{\text{background}})/(\text{OD}_{\text{control}} - \text{OD}_{\text{background}}) \times 100\%$$

IC50 values were calculated in GraphPad Prism 9.0 using nonlinear regression (four-parameter logic model).

### Cell apoptosis

Cell apoptosis was detected using the Annexin V-FITC/PI double staining kit (Nanjing KeyGen Biotech Co., Ltd.). Cells in logarithmic growth phase were seeded into 6-well plates ($5 \times 10^5$ cells per well). After reaching 70–80% confluency, the culture medium was replaced with fresh medium containing different nanomaterials (at concentrations corresponding to the $IC_{50}$ value, based on cerium concentration), and the cells were incubated for 24 h. The cells were then collected and stained with Annexin V-FITC and PI according to the kit instructions. After incubation for 30 min at room temperature, the cells were detected using a flow cytometer.

Apoptosis was also detected using the TUNEL kit. First, the cells were fixed with 4% paraformaldehyde, then washed with PBS. Subsequently, PBS containing 0.3% Triton X-100 was added and incubated at room temperature for 5 min. Then, 50 μL of TUNEL detection solution was added to the samples and incubated at 37℃ in the dark for 60 min. After washing with PBS three times, the samples were mounted with an anti-fade mounting medium and observed under a fluorescence microscope (Olympus microscope).

### Wound healing assay

The migration and proliferation abilities of MB49 cells were assessed using the scratch assay[25]. Approximately $5 \times 10^5$ cells were seeded per well in 6-well plates to achieve a confluency of 50–60%, followed by overnight incubation. Under sterile conditions, three straight scratches were made per well using a 200 μL pipette tip guided by a ruler. The medium was then replaced to remove dislodged cells. Images were captured at 100X magnification and recorded as the 0-hour time point. Afterward, treatments were administered according to the experimental groups and incubated for 24 h. Following incubation, the medium was replaced with fresh medium, and images were captured again at 100X magnification to be recorded as the 24-hour time point. The migration distance was quantified using ImageJ software.

### Cell cycle assay

Approximately $5 \times 10^5$ cells were seeded per well in 6-well plates to achieve a confluency of 70–80%, they were digested with trypsin, and the cells treated with different nanomaterials (at concentrations corresponding to the $IC_{50}$ value, based on cerium concentration) were collected. After washing with PBS, the cells were resuspended in 1 mL of ice-cold 70% ethanol, Gently vortexed to mix, and fixed at 4℃ for 30 min. The cells were then centrifuged, washed, and resuspended. Propidium iodide staining solution (25 uL) was added, and the cells were incubated at 37℃ in the dark for 30 min. Finally, the cells were analyzed using flow cytometry.

### EdU assay

Cells were seeded in 12-well plates at a density of approximately $1 \times 10^5$ cells per well to achieve 50–60% confluency, followed by overnight culture prior to subsequent experiments. The compounds were applied at their respective $IC_{50}$ concentrations, and an equal volume of 2X EdU working solution was added for incubation. After removing the culture medium, cells were fixed with paraformaldehyde for 15 min. The paraformaldehyde was then removed, and 1 mL of PBS containing 0.3% Triton X-100 was added to each well and incubated at room temperature for 10–15 min. After washing, Click reaction solution was added, mixed well, and incubated at room temperature in the dark for 30 min. Subsequently, 1X Hoechst 33,342 solution was added to each well for incubation. After washing, the cells were subjected to fluorescence detection.

### GSH/GSSG ratio assay protocol

The GSH and GSSG Assay Kit is used to quantify the levels of glutathione in its reduced (GSH) and oxidized (GSSG) forms. A decrease in the GSH/GSSG ratio is widely recognized as a gold standard indicator of ferroptosis. Reduced glutathione serves as a critical antioxidant. According to the manufacturer's instructions, intracellular GSH and GSSG levels were measured using standard curves, and the GSH/GSSG ratio was subsequently calculated. A decreased GSH/GSSG ratio is associated with increased apoptosis and inhibition of cell growth.

### qPCR detection

First, nucleic acid extraction was performed. RNA was extracted from MB49 cells treated with different nanomaterials, and the concentration was measured. Subsequently, reverse transcription was carried out to convert the RNA samples into cDNA. Total RNA was extracted from cellsusing TRIzol® Reagent (Invitrogen), following the manufacturer's protocol. Complementary DNA (cDNA) was synthesized from 1 μg of total RNA using the PrimeScript™ RT Reagent Kit (Takara Bio) with oligo(dT) and random hexamer primers, according to the manufacturer's instructions. After purification, the cDNA was amplified using specific primers and probes. The relative expression of the genes was then detected and calculated. The qPCR reaction system and thermal cycling conditions were as follows: denaturation, 95 °C for 5 s, annealing/extension, 60 °C for 30 s. After amplification, a melting curve was Generated by heating from 60 °C to 95 °C to confirm primer specificity.

## Western blot

A cell suspension with approximately $5 \times 10^5$ cells per well was seeded in a 6-well plate and incubated overnight or for 24 h to allow cell attachment and growth for subsequent experiments. The culture medium was then replaced to remove impurities, followed by the addition of nanomaterials at concentrations corresponding to their IC50 values. After 24 h of incubation, cell samples were collected for protein extraction. The proteins were separated by SDS-PAGE and then transferred onto a PVDF membrane. After blocking the membrane, it was incubated with specific primary antibodies, followed by incubation with horseradish peroxidase-conjugated secondary antibodies. The protein bands were visualized using an Enhanced ChemiLuminescenc (ECL) substrate.

## Statistical analysis

All data are presented as the mean ± standard deviation (SD) of at least three independent experiments. Statistical analyses were performed using GraphPad Prism software. Statistical analysis was based on a one-way analysis of variance and Student' s tests. The significance levels were defined as follows: $*p < 0.05$, $**p < 0.01$, $***p < 0.001$, and ns (not significant) for no statistical significance.

## Results and discussion

### Synthesis and characterization of Au/CeO$_2$@As NPs

In the presence of strong oxidizing ammonium, Au/CeO$_2$ nanoparticles were synthesized through the auto-redox reaction of AuCl4$^-$ and Ce$^{3+}$, with the specific synthesis steps shown in Fig. 1A. Transmission electron microscopy (TEM) images revealed that Au/CeO$_2$@As exhibited a core-shell nanostructure with a particle size of approximately 20 nm (Fig. 1B). Further studies on the hydrodynamic size and zeta potential of the
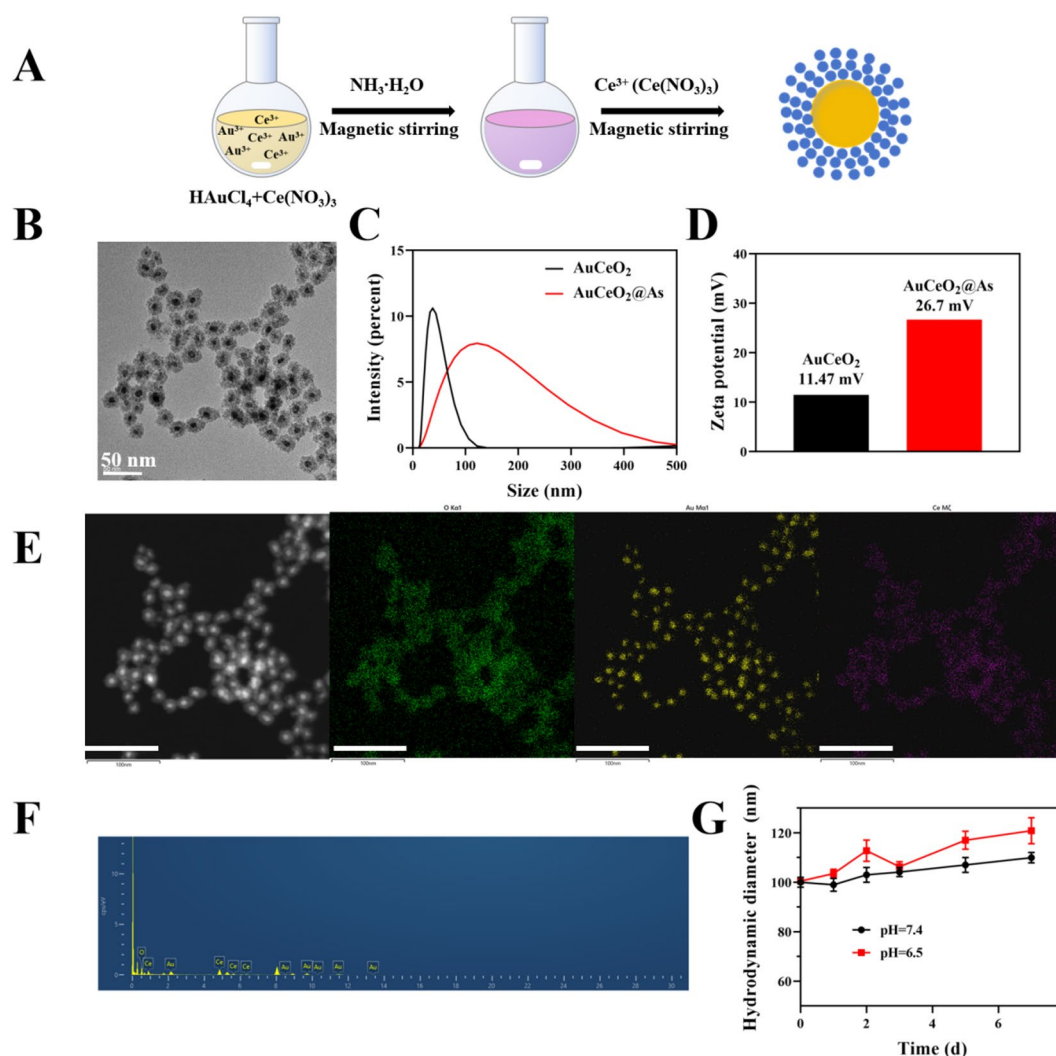


**Fig. 1**. Characterization of Au/CeO$_2$@As. (**A**) Schematic illustration of the Au/CeO$_2$@As. (**B**) TEM image of Au/CeO$_2$@As. (**C**) DLS measurement of nanoparticles in water. (**D**) The Zeta potential of nanoparticles at different fabrication stages was measured at 25 °C. (**E**) EDS element mappings of Au/CeO$_2$@As. Scale bar = 100 nm. (**F**) EDS of Au/CeO$_2$@As.(**G**) Characterization of Au/CeO$_2$@As stability.

nanoparticles were conducted using dynamic light scattering (DLS) experiments (Fig. 1C, D). We found that the hydrodynamic size of Au/CeO$_2$@As NPs was approximately $98.52 \pm 23.8$ nm, with a zeta potential of about 26.7 mV. These values changed significantly compared to those before the loading of astragaloside (Au/CeO$_2$ hydrodynamic size: $40.81 \pm 10.4$ nm, zeta potential: approximately 11.47 mV), indicating the successful synthesis of Au/CeO$_2$@As NPs. Additionally, energy-dispersive X-ray spectroscopy (EDS) elemental mapping confirmed that Au elements were mainly distributed in the core of the nanoparticles, while Ce and O elements were uniformly distributed (Fig. 1E, F). EDS spectroscopy (Fig. S1) clearly revealed the atomic percentages of O, Ce, and Au to be 20.74%, 57.95%, and 21.31%, respectively. The fact that these three signals originated from the same region provides compelling evidence for the successful synthesis of the composite nanomaterial. In addition, HPLC analysis showed that the drug loading of As-IV was about 63.5% (Fig. S2). Meanwhile, the stability of the Au/CeO$_2$@As nanoparticles was evaluated by monitoring the time-dependent changes in their hydrodynamic size under different conditions. As shown in Fig. 1G, the hydrodynamic diameter of the nanoparticles remained largely unchanged under neutral conditions over 7 days, indicating good stability. In contrast, under acidic conditions, cerium dioxide tended to aggregate due to alterations in surface charge, leading to noticeable changes in nanoparticle size[26–28]. Furthermore, the stability of the nanoparticles was also assessed in DMEM culture medium. The results demonstrated that the nanoparticles maintained considerable stability over a period of 72 h (Fig. S3).

### Cytotoxicity of Au/CeO$_2$@As NPs

We investigated the cytotoxicity of Au/CeO$_2$@As NPs using the CCK-8 assay and the Calcein-AM/PI Live/Dead Cell Double Stain Kit. As shown in Fig. 2A, compared with the control group, the addition of Au/CeO$_2$ slightly inhibited cell growth, but the effect was not significant. Astragaloside A significantly suppressed cell growth and increased the number of dead cells. However, the Au/CeO$_2$@As group exhibited a more pronounced increase in dead cells, with a marked rise in red fluorescence (dead cells), indicating an interaction that enhanced the killing
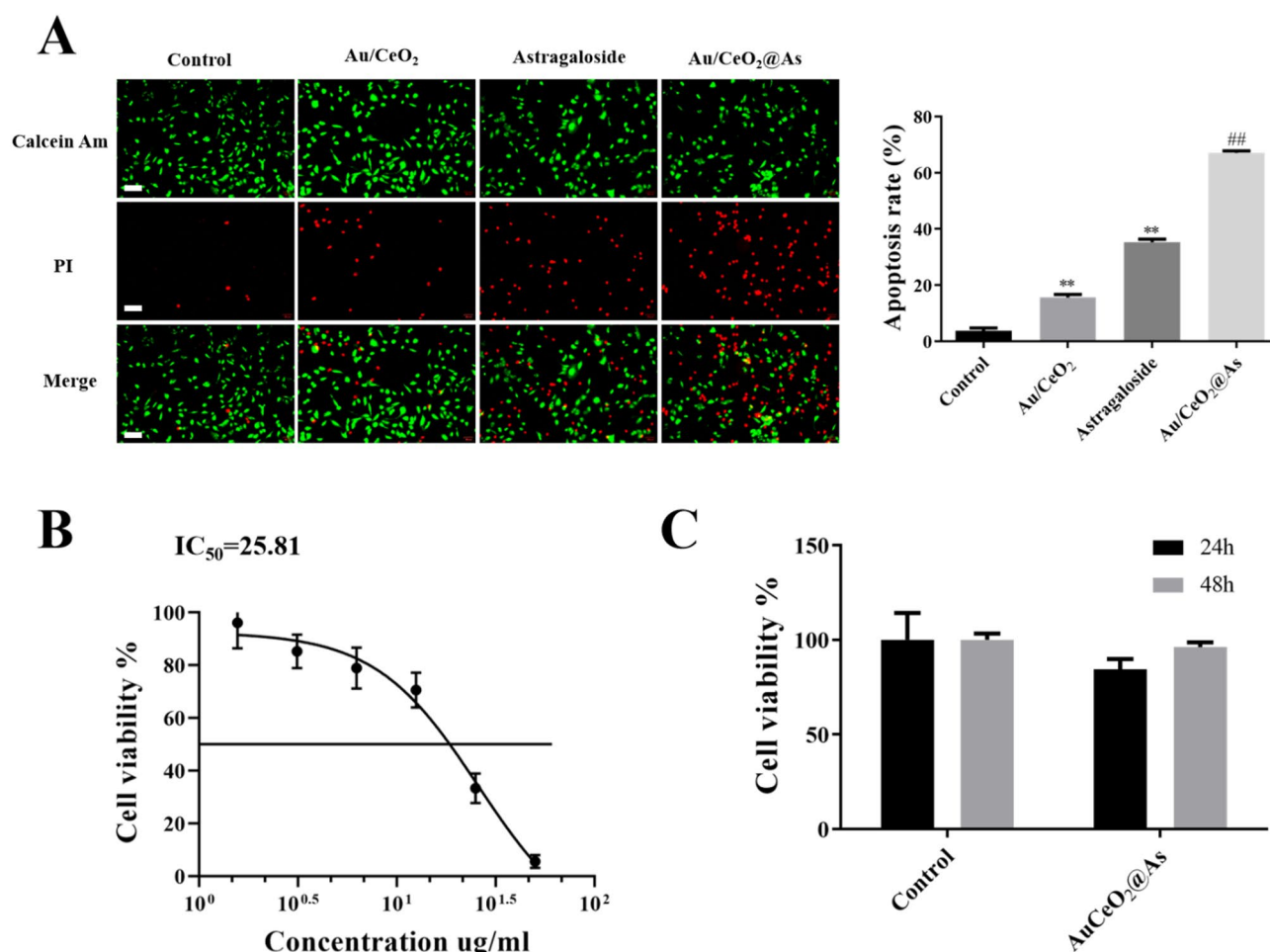


**Fig. 2.** In *vitro* antitumor activity. (**A**) Fluorescence images of MB49 cells after treatment with nanoparticles, live cells stained with Calcein-AM produce strong green fluorescence; dead cells stained with PI form bright red fluorescent. Scale bar = 50 μm. (**B**) MB49 cells after being treated with nanoparticles determined by CCK-8 assay. (**C**) Normal cells after being treated with nanoparticles determined by CCK-8 assay. (#, $p < 0.05$; ##, $p < 0.01$, *$p < 0.05$, **$p < 0.01$).

capability against tumor cells. Next, we determined the $IC_{50}$ value of Au/CeO$_2$@As NPs using the CCK-8 assay (Fig. 2B). As illustrated, after incubating MB49 cells with varying concentrations of Au/CeO$_2$@As NPs, we found that the half-maximal inhibitory concentration ($IC_{50}$) was 25.81 μg/mL, meaning that at this concentration, half of the MB49 cells were killed. Additionally, we evaluated the toxicity of Au/CeO$_2$@As NPs on normal cells (Fig. 2C). The results showed that, whether incubated for 24–48 h, the cell viability remained largely unchanged, maintaining approximately 90%, suggesting that the NPs had no significant inhibitory effect on normal cell growth. In summary, these findings demonstrate that Au/CeO$_2$@As NPs possess specific tumor-killing ability while exhibiting good biosafety.

## Cell apoptosis

We evaluated the inhibitory effect of Au/CeO$_2$@As NPs on MB49 cells by detecting apoptosis using Annexin V and propidium iodide (PI) staining, with the results shown in Fig. 3A. The findings revealed that, compared to other drug-treated groups, the Au/CeO$_2$@As group significantly enhanced apoptosis in MB49 cells. Specifically, the apoptosis rate in the control group was only 0.66%, while the rates induced by Au/CeO$_2$, As-IV, and Au/CeO$_2$@As were 0.71%, 1.64%, and 3.37%, respectively. These results indicate that As-IV alone has a certain ability to induce apoptosis in MB49 cells, but Au/CeO$_2$@As induced a more pronounced apoptotic effect, demonstrating the therapeutic potential of the combination in bladder cancer treatment.

Furthermore, we investigated MB49 cell apoptosis using the TUNEL assay (Fig. 3B). Compared with the control group, Au/CeO$_2$ treatment increased green fluorescence, while As-IV alone induced even more noticeable fluorescence. However, the Au/CeO$_2$@As group exhibited the most intense green fluorescence, indicating a higher level of apoptosis. Figure 3C provides a more intuitive observation, confirming that Au/CeO$_2$@As induced significantly more apoptosis than the other treatments. In conclusion, Au/CeO$_2$@As nanoparticles exhibit a synergistic effect, demonstrating enhanced tumor cell-killing capability.

## Inhibitory effects of Au/CeO$_2$@As nanoparticles on cell proliferation

Nanomaterials, with their unique physicochemical properties such as small size effect, high specific surface area, and targeting modification capabilities, have demonstrated significant advantages in the field of anti-tumor applications[29,30]. In the acidic tumor microenvironment, CeO$_2$ exhibits peroxidase (POD)-like activity, catalyzing the decomposition of H$_2$O$_2$ into highly toxic hydroxyl radicals (·OH), which induce oxidative damage and suppress cell proliferation[31]. Similarly, Au nanoparticles can trigger oxidative stress, leading to DNA damage, cell cycle disruption, and inhibition of cell proliferation[32]. To further investigate the cell proliferation inhibitory effects of Au/CeO$_2$@As NPs, we conducted a series of comprehensive assays. These experiments were designed to evaluate their synergistic mechanisms in inducing oxidative stress, DNA damage, and cell cycle arrest, thereby enhancing their antitumor efficacy. The results demonstrate that the combination of Au/CeO$_2$ and As-IV not only amplifies reactive oxygen species (ROS) generation but also reinforces cell cycle blockade, providing a more effective strategy for tumor suppression.

First, we employed the wound-healing assay—a straightforward and intuitive in vitro method—to evaluate cell proliferation and migration capabilities. The results are shown in Fig. 4A. Compared to the control group, Au/CeO$_2$ exhibited a certain inhibitory effect on cell migration and proliferation, while As-IV demonstrated a more pronounced suppression of MB49 cell migration and proliferation. However, in the Au/CeO$_2$@As NPs
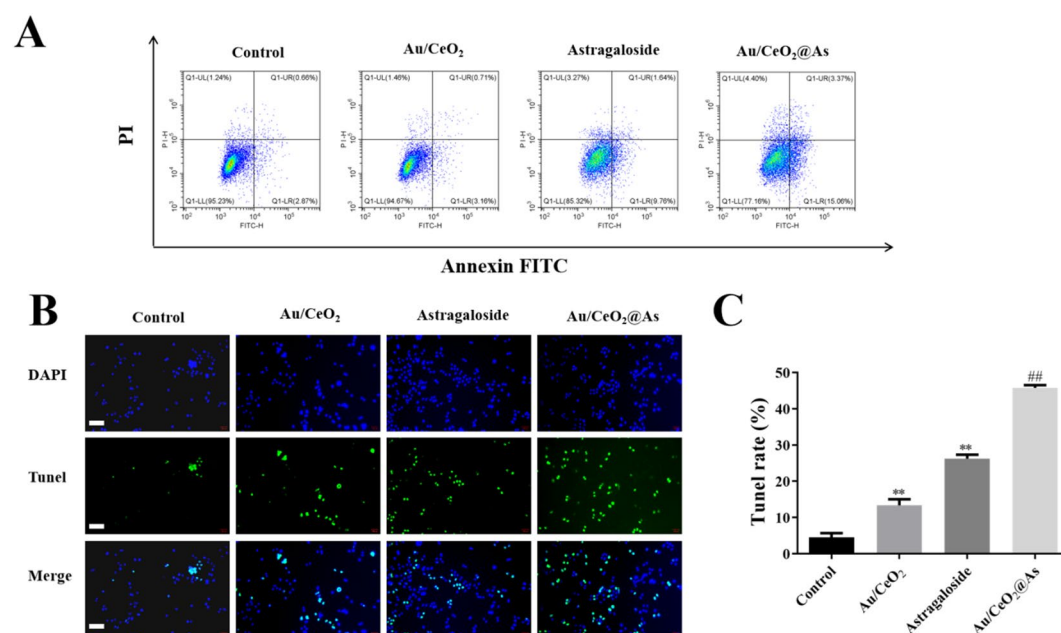


**Fig. 3.** Apoptosis detection. (**A**) Apoptosis of MB49 cells detected by flow cytometry. (**B, C**) TUNEL staining of MB49 cells shows the different apoptosis. (#, $p < 0.05$; ##, $p < 0.01$, *$p < 0.05$, **$p < 0.01$). Scale bar = 50 μm.
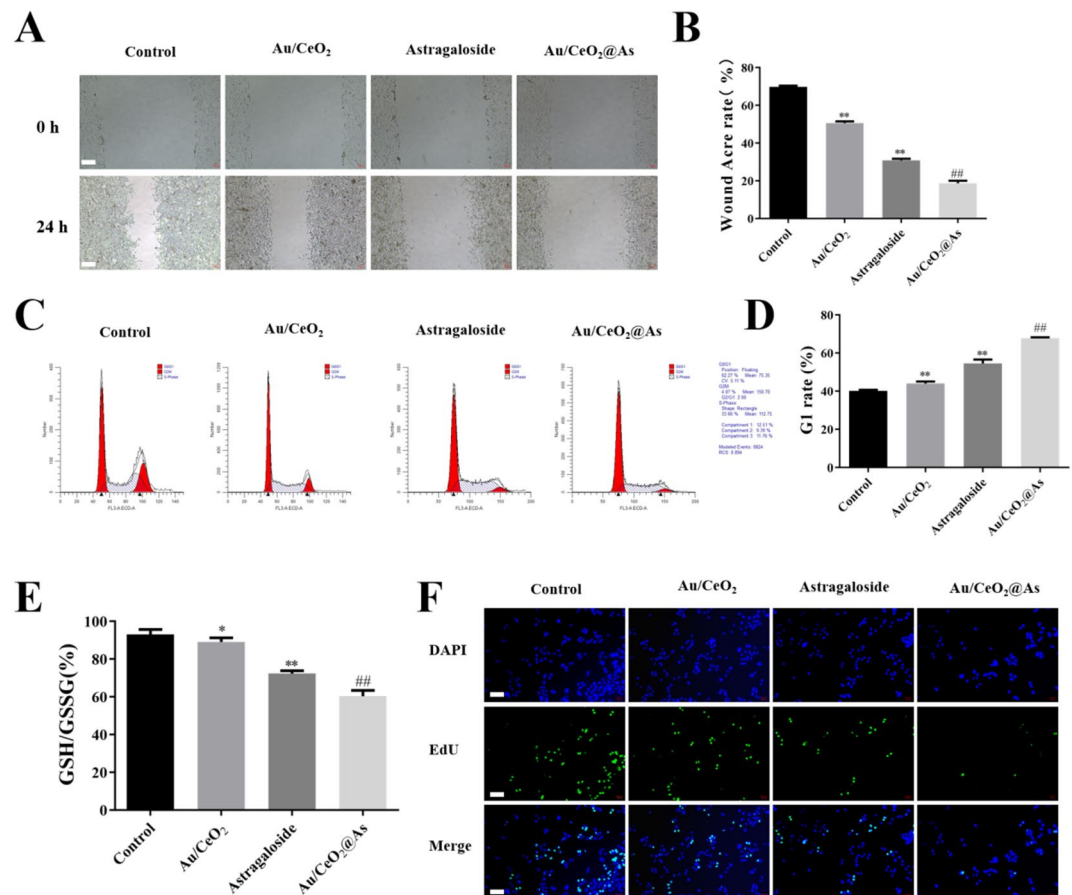
**Fig. 4**. Cell proliferation inhibition test. (**A**) Representative images of scratch wounds post-scratching. Scale bar = 50 μm. (**B**) Quantification of wound closure rate (mean ± SD, $n = 3$). (**C**) Flow cytometry histograms showing DNA content (PI staining) treatment. (**D**) Quantitative analysis of cell population in G0/G1, S, and G2/M phases (mean ± SD, $n = 3$). (one-way ANOVA). (**E**) Calculated GSH/GSSG ratio (mean ± SD, $n = 3$). (**F**) Representative images: EdU$^+$ cells (green, Click-iT chemistry), nuclei (blue, DAPI). Scale bar = 50 μm. (#, $p < 0.05$; ##, $p < 0.01$, *$p < 0.05$, **$p < 0.01$).

group, MB49 cells showed almost no migration or proliferation. Figure 4B further highlights the significantly stronger inhibitory effect of Au/CeO$_2$@As, indicating that the combination of Au/CeO$_2$ and As-IV produces a synergistic effect superior to either treatment alone. Next, we further assessed cell proliferation inhibition by examining the cell cycle. The cell cycle is a fundamental process governing cell growth and division, and its precise regulation is crucial for maintaining tissue homeostasis. In tumor development, dysregulation of the cell cycle is a key mechanism driving uncontrolled cancer cell proliferation[33]. As shown in Fig. 4C and D, compared to the control group, treatment with Au/CeO$_2$ led to a slight but insignificant increase in the proportion of cells arrested in the G1 phase, indicating mild growth suppression. In contrast, As-IV alone induced a more significant G1-phase accumulation, demonstrating its stronger inhibitory effect on cell cycle progression.

However, Au/CeO$_2$@As NPs triggered a far more pronounced G1-phase arrest, with a substantially higher proportion of cells stalled in G1. This G1 blockade prevents cells from passing the G1/S checkpoint and entering the S phase, ultimately halting proliferation. Since the G1/S transition is critical for DNA replication and cell division, its inhibition forces tumor cells into senescence or apoptosis, thereby achieving an enhanced anti-tumor therapeutic effect. These findings further confirm that Au/CeO$_2$@As NPs exert a synergistic cell cycle arrest mechanism, surpassing the individual effects of Au/CeO$_2$ or As-IV alone. This dual-action strategy—combining nanoparticle-induced oxidative stress with phytochemical-mediated cell cycle disruption—provides a more effective approach to suppressing tumor growth[34]. Figure 4D illustrates the result more clearly. Furthermore, we quantified the distribution of cells across different cell cycle phases (Fig.S4). The results demonstrated that the addition of Au/CeO$_2$@As led to an increased proportion of cells in the G1 phase, which arrested cell division and prevented their progression to the next cycle, thereby inhibiting cell growth. This observation is consistent with the findings described previously.

In addition, a lower GSH/GSSG ratio induces cell cycle arrest or apoptosis, which can be used in anti-tumor strategies[35]. Therefore, we further assessed the inhibitory effect of Au/CeO$_2$@As nanoparticles on cell proliferation using the GSH/GSSG Detection Assay Kit, with the results shown in Fig. 4E. The results indicated that after treatment with Au/CeO$_2$@As nanoparticles, the GSH/GSSG ratio significantly decreased compared
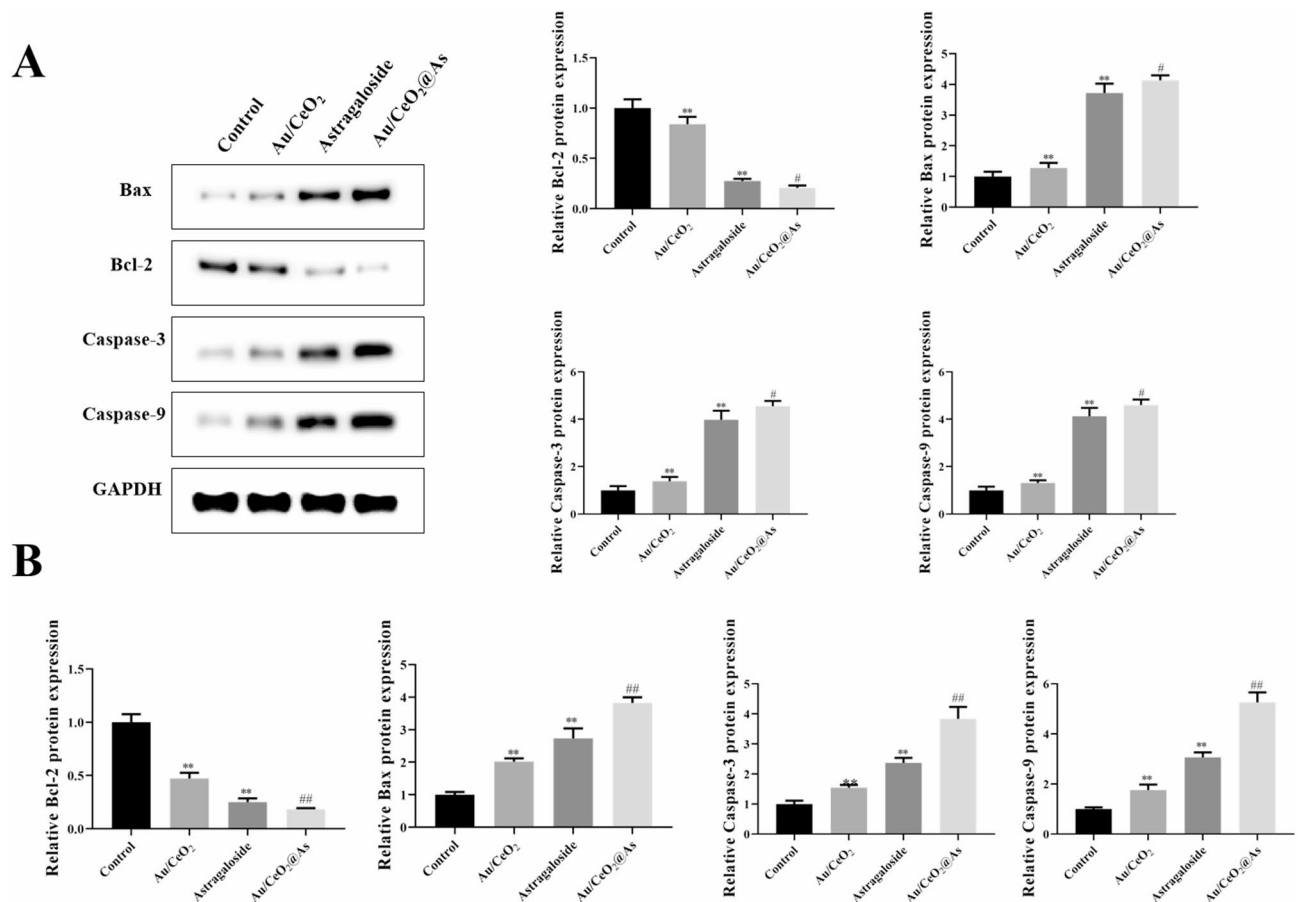
**Fig. 5**. (**A**) Western blot analysis and densitometric quantification (mean ± SD, $n = 3$). (**B**) q-PCR analysis of Bcl-2, Bax, Caspase-3, and Caspase-9. (#, $p < 0.05$; ##, $p < 0.01$, *$p < 0.05$, **$p < 0.01$).

to the control group, suggesting that cell proliferation was inhibited and the nanoparticles exhibited strong tumor-killing ability. Depletion of GSH leads to the accumulation of reactive oxygen species (ROS), which activates the p53-p21 pathway, causing cell cycle arrest at the G1 phase. Elevated GSSG can oxidatively modify histone deacetylases (HDACs), thereby inhibiting the expression of proliferation-promoting genes. Therefore, when the GSH/GSSG ratio decreases, cell proliferation is inhibited, achieving the effect of tumor killing and demonstrating therapeutic potential for bladder cancer[35]. We also detected cells in the S phase using the EdU (5-ethynyl-2'-deoxyuridine) method, with the results shown in Fig. 4F. The EdU assay is used to study the proliferation of individual cells. From the results, we found that astragaloside can inhibit cell proliferation, but the synergistic effect of Au/CeO$_2$@As enhances the inhibition of cell growth. Based on the comprehensive analysis above, we concluded that Au/CeO$_2$@As nanoparticles can achieve the effect of tumor treatment by inhibiting cell proliferation.

## Inhibition of STAT3 and NF-κB signaling pathways

As-IV, the primary active component of Astragalus membranaceus, exhibits multi-target therapeutic effects. Research indicates that it bidirectionally regulates apoptosis by modulating the Bcl-2/Bax protein ratio and inhibiting the Caspase-3/9 pathway: it induces apoptosis in cancer cells while exerting anti-apoptotic protective effects in the cardiovascular and nervous systems[36]. This selective apoptosis regulation gives it unique advantages in treating various diseases, particularly showing significant potential in reducing chemotherapy side effects[21,37]. Our research findings indicate that Au/CeO$_2$ nanoparticles induce cell apoptosis by generating reactive oxygen species (ROS), while As-IV triggers apoptosis by modulating signaling pathways. The synergistic action of these two components enhances the killing effect on tumor cells. To evaluate the expression of apoptosis-related proteins in MB49 cells, we performed q-PCR and Western blotting assays for Bcl-2, Bax, Caspase-3, and Caspase-9. Both Western blot (Fig. 5A) and q-PCR (Fig. 5B) results consistently showed that Au/CeO$_2$@As significantly downregulated the anti-apoptotic protein Bcl-2, while upregulating the pro-apoptotic protein Bax and the executioner proteins Caspase-3 and Caspase-9 compared to As-IV alone. This dual mechanism of action endows Au/CeO$_2$@As with a stronger capacity to kill tumor cells.

Our findings demonstrate that the Au/CeO$_2$@As NP platform exhibits a unique multi-modal mechanism of action that distinguishes it from conventional cancer therapies. Compared to traditional chemotherapy (e.g., paclitaxel, doxorubicin), which relies on non-specific cytotoxicity towards all rapidly dividing cells, our nano-

formulation leverages the enhanced permeability and retention (EPR) effect to achieve preferential accumulation in tumor tissue[38,39]. This passive targeting strategy aims to reduce the systemic, off-target toxicity that is the primary dose-limiting factor of chemotherapy. While chemotherapy drugs often induce apoptosis through direct DNA damage or microtubule disruption, our approach utilizes As-IV to modulate specific apoptotic pathways (Bcl-2/Bax ratio, Caspase-3/9), potentially offering a more regulated induction of cell death and mitigating the severe side effects (e.g., bone marrow suppression, neurotoxicity) commonly associated with chemo drugs[40,41]. The most significant differentiator is the bidirectional regulation of apoptosis. Unlike most chemotherapies and targeted drugs that are solely cytotoxic, As-IV has been documented to induce apoptosis in cancer cells while protecting certain normal cells[42]. This aligns perfectly with our data showing significant cytotoxicity in MB49 cancer cells but negligible harm to normal cells. This selective toxicity is the cornerstone of a wider therapeutic window, which is the ultimate goal in oncology drug development. This stands in stark contrast to the narrow therapeutic index of many conventional therapies. In addition, the nano-platform addresses key challenges in the delivery of natural bioactive compounds like As-IV, which often suffer from poor solubility, low bioavailability, and non-specific distribution.

However, translating these promising in vitro results into the clinic requires overcoming several challenges. Future work must include extensive in vivo studies using immunocompetent animal models to validate efficacy, pharmacokinetics, and long-term biosafety. The scale-up of nanoparticle synthesis with good manufacturing practice (GMP) standards and a thorough investigation of potential immunogenicity are also critical steps toward clinical application. However, the above limitations do not affect the current conclusions, although further experimental studies are needed in the future.

## Conclusion

This study developed a novel gold nanoparticle-embedded cerium nanozyme loaded with As-IV (Au/CeO$_2$@As) for bladder cancer treatm Research indicates that ent. In vitro experiments confirmed that this nanosystem exerts anti-tumor effects through a dual mechanism: on one hand, the Au/CeO$_2$ nanocarrier itself exhibits tumor proliferation-inhibiting activity, while on the other hand, the loaded As-IV significantly enhances tumor cell-killing effects by regulating apoptotic signaling pathways (Bcl-2/Bax and Caspase-3/9). Although the absolute efficacy, such as the IC$_{50}$ value, is moderate compared to some first-line chemotherapeutics, the observed selective toxicity is a promising finding. These results represent a proof-of-concept that our nano-strategy can improve the bioactivity of As-IV. However, their ultimate therapeutic relevance and potential for clinical translation must be rigorously evaluated in future studies through more complex in vivo models and detailed mechanistic investigations.

## Data availability

All data generated or analysed during this study are included in this published article (and its Supplementary Information files).

## References

1. Flaig, T. W. et al. Bladder cancer. Version 3.2020. *J. Natl. Comper Can. Net.* **18** (3), 329–354 (2020).
2. Gotlib, J. et al. NCCN Guidelines® Insights: Systemic Mastocytosis, Version 3.2024. *J. Natl. Compr. Can. Net. 22* (2D). (2024).
3. Facchini, G., Romis, C. C. L., Lei, K. F. & Han, F. Advanced/metastatic bladder cancer: current status and future directions. *Eur. Rev. Med. Pharmaco Sci.* **24**, 11536–11552 (2020).
4. Flaig, T. W. et al. Bladder cancer, version 3.2024 featured updates to the NCCN guidelines. *J. Natl. Compr. Can. Net.* **22** (4), 216–225 (2024).
5. Desai, A. P. et al. Financial conflicts of interest among National comprehensive cancer network clinical practice guideline panelists in 2019. *Cancer* **126** (16), 3742–3749 (2020).
6. Babjuk, M. et al. EAU guidelines on non-muscle-invasive urothelial carcinoma of the bladder. *Eur. Urol.* **54** (2), 303–314 (2008).
7. Dobruch, J. & Oszczudlowski, M. Bladder cancer: current challenges and future directions. *Med-Lith* **57** (8), 749–758 (2021).
8. Karjol, U., Jonnada, P., Cherukuru, S. & Chandranath, A. Bladder metastasis from breast cancer: A systematic review. *Cur J. Med. Sci* **12** (3), e7408 (2020).
9. Douglass, L. & Schoenberg, M. The future of intravesical drug delivery for Non-Muscle invasive bladder cancer. *Bladder Cancer (Amsterdam Netherlands).* **2** (3), 285–292 (2016).
10. Wang, L. et al. Myeloid Cell-associated resistance to PD-1/PD-L1 Blockade in urothelial cancer revealed through bulk and Single-cell RNA sequencing. *Clin. Can. Res. : Official J. Am. Association Cancer Res.* **27** (15), 4287–4300 (2021).
11. Gill, E. & Perks, C. M. Mini-Review: current bladder cancer Treatment-The need for improvement. *Int J. Mol. Sci* **25** (3), 1557–69 (2024).
12. Begines, B. et al. Polymeric nanoparticles for drug delivery: recent developments and future prospects. *Nanomaterials* **10**, 7 (2020).
13. Ashrafizadeh, M. et al. Nanoplatforms in bladder cancer therapy: challenges and opportunities. *Bio Transl Med* **8** (1), e10353 (2023).
14. Yoon, H. Y. et al. Current status of the development of intravesical drug-delivery systems for the treatment of bladder cancer. *Exp. Opin. Dru Del.* **17** (11), 1555–1572 (2020).
15. GuhaSarkar, S. & Banerjee, R. Intravesical drug delivery: challenges, current status, opportunities and novel strategies. *J. Control Rel.* **148** (2), 147–159 (2010).
16. Huang, Y. Q. et al. Cationic conjugated Polymer/Hyaluronan-Doxorubicin complex for sensitive fluorescence detection of hyaluronidase and Tumor-Targeting drug delivery and imaging. *ACS Appl. Mater. Inter.* **7** (38), 21529–21537 (2015).
17. Bai, X. et al. An NIR-propelled Janus nanomotor with enhanced ROS-scavenging, Immunomodulating and biofilm-eradicating capacity for periodontitis treatment. *Bio Mater.* **41**, 271–292 (2024).
18. Ge, K. et al. Gold nanorods with Spatial separation of CeO$_2$ deposition for Plasmonic-Enhanced antioxidant stress and photothermal therapy of alzheimer's disease. *ACS Appl. Mater. Inter.* **14** (3), 3662–3674 (2022).
19. Babu, B. et al. Inorganic nanoparticles as radiosensitizers for cancer treatment. *Nanomaterils* **13**, 21 (2023).

20. Zhang, D. et al. Design of 3D Oxide-Metal hybrid metamaterial for tailorable Light-Matter interactions in visible and Near-Infrared region. *Adv Optl Mater* **9** (1), 1–11 (2021).
21. Chen, Y., Zhang, W. & Huang, Y. The therapeutic effect of Methotrexate-Conjugated Pluronic-Based polymeric micelles on the folate Receptor-Rich tumors treatment (Retraction of 10, Pg 4043, 2015). *Inter J. Nanomed.* **17**, 5601–5601 (2022).
22. Yao, M., Zhang, L. J., Wang, L. & Astragaloside, I. V. A promising natural neuroprotective agent for neurological disorders. *Bio Pharma* **159**, 114229 (2023).
23. Kong, C. et al. A tumor targeted nano micelle carrying Astragaloside IV for combination treatment of bladder cancer. *Sci Rep* **14** (1), 17704 (2024).
24. Li, J. et al. Investigating the Hybrid-Structure-Effect of $CeO_2$-Encapsulated Au nanostructures on the transfer coupling of nitrobenzene. *Advan Mater* **30** (7), 1704416 (2018).
25. Liang, C. C. & Park, A. Y. Jun-Lin Guan. In vitro scratch assay: a convenient and inexpensive method for analysis of cell migration in vitro. *Nat. Protoc.* **2**, 329–3 (2007).
26. Axson, J. L. et al. Rapid kinetics of size and pH-Dependent dissolution and aggregation of silver nanoparticles in simulated gastric fluid. *J. Physi Chem. C.* **119** (35), 20632–20641 (2015).
27. Peretyazhko, T. S., Zhang, Q. & Colvin, V. L. Size-Controlled dissolution of silver nanoparticles at neutral and acidic pH conditions: kinetics and size changes. *Environ. Sci. Tech.* **48** (20), 11954–11961 (2014).
28. Cui, C. et al. Functional Ginger-Derived extracellular Vesicles-Coated ZIF-8 containing TNF-α SiRNA for ulcerative colitis therapy by modulating gut microbiota. *ACS Appl. Mater. Inter.* **16** (40), 53460–53473 (2024).
29. Choi, E., Lim, D. K. & Kim, S. Calcium-doped mesoporous silica nanoparticles as a lysosomolytic nanocarrier for amine-free loading and cytosolic delivery of SiRNA. *J. Ind. Engin Chem.* **81**, 71–80 (2020).
30. Chen, A. M. et al. Co-delivery of doxorubicin and Bcl-2 SiRNA by mesoporous silica nanoparticles enhances the efficacy of chemotherapy in Multidrug-Resistant cancer cells. *Small* **5** (23), 2673–2677 (2009).
31. Wang, D. et al. Synthesis of Self-Assembled porphyrin nanoparticle photosensitizers. *ACS Nano.* **12** (4), 3796–3803 (2018).
32. Sucharitakul, S. et al. Intrinsic electron mobility exceeding in multilayer InSe fets. *NANO Lett.* **15** (6), 3815–3819 (2015).
33. Chen, J. The Cell-Cycle arrest and apoptotic functions of p53 in tumor initiation and progression. *CSH Perspe Med* **6** (3), a026104 (2016).
34. Zhang, Y. et al. O-GlcNAcylation of MITF regulates its activity and CDK4/6 inhibitor resistance in breast cancer. *Nat Commun* **15** (1), 5597 (2024).
35. Zhang, R. et al. Pyridinic Nitrogen Sites Dominated Coordinative Engineering of Subnanometric Pd Clusters for Efficient Alkynes' Semihydrogenation. *Adv Mater* **35** (11), e2209635 (2023).
36. cHEN, T. I. A. N. Q. I. & a., P. Y. Molecular mechanisms of astragaloside–IV in cancer therapy. *Inter J. Mol. Medic.* **47** (13), 1–13 (2021).
37. Noor, K. K. et al. Hepatoprotective role of vitexin against cadmium-induced liver damage in male rats: A biochemical, inflammatory, apoptotic and histopathological investigation. *Bio. Pharma.* 150. (2022).
38. Zi, Y. et al. Strategies to enhance drug delivery to solid tumors by Harnessing the EPR effects and alternative targeting mechanisms. *Adv. Drug Deliv Rev.* **188**, 114449 (2022).
39. Sun, R. et al. The tumor EPR effect for cancer drug delivery: current status, limitations, and alternatives. *Adv. Drug Deliv Rev.* **191**, 114614 (2022).
40. Monsuez, J. J., Charniot, J. C., Vignat, N. & Artigou, J. Y. Cardiac side-effects of cancer chemotherapy. *Inter J. Cardio.* **144** (1), 3–15 (2010).
41. Stankovic, J. S. K., Selakovic, D., Mihailovic, V. & Rosic, G. Antioxidant supplementation in the treatment of neurotoxicity induced by Platinum-Based Chemotherapeutics—A review. *Inter J. Mol. Sci.* **21**, 20 (2020).
42. Li, Z. et al. Tanshinone IIA and astragalosideï IV promote the angiogenesis of mesenchymal stem cell-derived endothelial cell-like cells via upregulation of Cx37, Cx40 and Cx43. *Exp Thera Med.***15**, 1847–1854 (2017).

## Acknowledgements

## Author contributions

Z. Data curation, Formal analysis, Investigation, Writing-Original Draft, Y. N. Formal analysis, Investigation, Writing-Original Draft, Y. X. Formal analysis, Investigation, Y. C. M. Investigation, H. W. Project administration, Supervision, T. Conceptualization; Supervision; Funding acquisition; Writing-Review & Editing; Project administration.

## Declarations

## Competing interests

The authors declare no competing interests.

## Additional information

**Supplementary Information** The online version contains supplementary material available at https://doi.org/10.1038/s41598-025-20068-9.

**Correspondence** and requests for materials should be addressed to F.T.

**Reprints and permissions information** is available at www.nature.com/reprints.

**Publisher's note** Springer Nature remains neutral with regard to jurisdictional claims in published maps and institutional affiliations.